

Collective Flow Enhancement by Tandem Flapping Wings

Nick Gravish,^{1,2} Jacob M. Peters,² Stacey A. Combes,³ and Robert J. Wood¹

¹SEAS, Harvard University, Cambridge, Massachusetts 02138, USA

²OEB, Harvard University, Cambridge, Massachusetts 02138, USA

³NPB, University of California Davis, Davis, California 95616, USA

(Received 15 January 2015; revised manuscript received 28 May 2015; published 27 October 2015)

We examine the fluid-mechanical interactions that occur between arrays of flapping wings when operating in close proximity at a moderate Reynolds number ($Re \approx 100\text{--}1000$). Pairs of flapping wings are oscillated sinusoidally at frequency f , amplitude θ_M , phase offset ϕ , and wing separation distance D^* , and outflow speed v^* is measured. At a fixed separation distance, v^* is sensitive to both f and ϕ , and we observe both constructive and destructive interference in airspeed. v^* is maximized at an optimum phase offset, ϕ_{\max} , which varies with wing separation distance, D^* . We propose a model of collective flow interactions between flapping wings based on vortex advection, which reproduces our experimental data.

DOI: 10.1103/PhysRevLett.115.188101

PACS numbers: 47.63.-b, 05.45.-a

Many biological and engineered systems rely on the control and movement of fluids. Fluid-structure interactions are ubiquitous in nature, and they have been studied extensively in the context of locomotory modes—such as flying and swimming—in which fluid flow generates the forces that underlie organismal motion [1–6]. In collective biological systems, fluid-structure interactions among groups may collectively affect the flow behavior. Fluid-mechanical interactions in collective systems have largely been considered for low Reynolds number flows, such as beating coral cilia [7,8], flapping flagella [9], and the run and tumble interactions of bacteria [10].

More recently, collective fluid-mechanical interactions have been examined for higher Reynolds number systems such as flocks of birds [11], schools of fish [12], flapping dragonfly wings [13–18], and other systems [19]. Collective fluid-structure interactions may be relevant to industrial applications such as wind farms [20], energy harvesting devices [21], and electronics cooling systems [22].

Here, we examine the effects of tandem wing flapping on collective fluid flow, inspired by the nest ventilation behaviors of honeybees (*Apis mellifera*). Honeybees regulate the carbon dioxide levels and temperature of their hives by collectively fanning their wings within the nest and at the entrance [23,24]. We have observed individual honeybees generating airflows up to 1.5 m/s, and maximum airflows exiting the hive entrance can be up to 4 m/s. During nest ventilation, honeybees arrange themselves in close proximity [Fig. 1(a)], often fanning immediately behind another fanning bee or a chain of bees. Inspired by this process, we seek to understand how wings flapping in close proximity affect the speed of the resulting airflow.

Fluid-structure interactions among pairs of flapping wings have been studied previously in the context of dragonfly flight [13–17]. Dragonflies possess pairs of fore- and hind wings that are controlled independently, and dragonflies display interwing phase differences that vary in different

flight contexts [16]. Reynolds-scaled physical models and numerical simulations on pairs of oscillating wings reveal that fluid interactions between the leading and trailing wings lead to varied lift production and power consumption as a function of the wing phase difference, ϕ [13–17].

Previous research on tandem wing interactions explored thrust generation as a function of wing phasing and separation. Here, we seek to understand how the induced

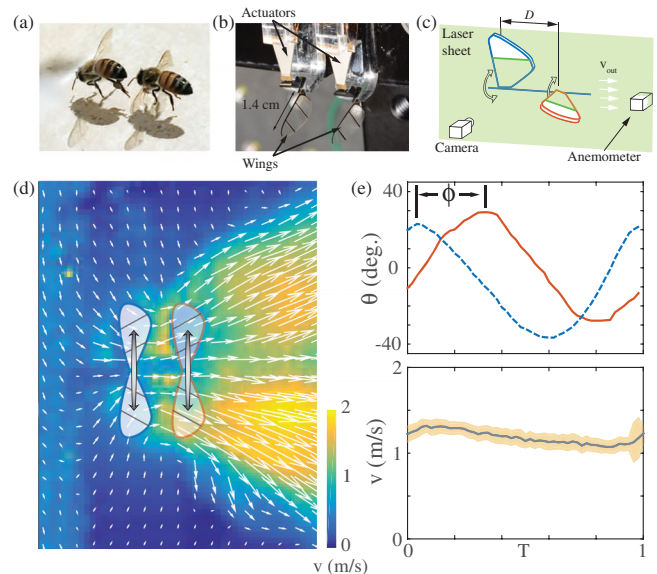


FIG. 1 (color online). Tandem wing experiments and biological inspiration. (a) Honeybees flap wings in close proximity for hive ventilation. (b) Lateral view of microfabricated tandem wings. (c) Experiment schematic showing laser and anemometer measurement. (d) Time averaged velocity field from a tandem wing array ($D^* = 0.2$). Color denotes velocity magnitude. (e) (Top panel) Stroke positional angle for leading (the dashed blue line) and trailing (the solid red line) wings. (Bottom panel) Outflow speed versus stroke period. Shaded region shows ± 1 s.d.

airflow is affected by wing phasing and other kinematic parameters. We studied arrays of flapping wings using an “at-scale” microrobotics platform [25], allowing us to vary the parameter space of control variables—flapping frequency f , amplitude θ_M , wing separation distance D^* , and phase ϕ —at the same Reynolds number as fanning honeybees.

Methods.—Flapping wing experiments were performed using microfabricated wing drivers constructed from carbon fiber and polymer sheets [25]. A piezoelectric actuator was connected to a hinge which drives the wing rotation [Fig. 1(b)]. An axial hinge aligned with the wing span direction allows for passive pitching rotation. Wing pitch angle is defined as 0° being horizontal and 90° vertical. Wing pitch trailed stroke positional angle with maximum pitch near midstroke (see the Supplemental Material [26], Fig. 1 and videos). Wings were vibrated at $f = 100$ Hz through peak-to-peak wing stroke amplitudes from $\theta_M = 30^\circ$ – 90° . Experiments were performed with two wing shapes of wing radius $R = 1.4$ cm and similar aspect ratios, 3.62 and 3.92 (with aspect ratio defined as R^2/S , where S is wing area), which displayed the same pattern of phase-dependent outflow speed. Phase-dependent flow was observed in both wing shapes (see the Supplemental Material [26]).

Fluid flow measurements were performed with a particle image velocimetry (PIV) system and a hot-wire anemometer. The PIV system consists of a 2W-continuous wave laser (532 nm, Dantec dynamics) imaged with a Phantom v7.3 high-speed camera (shutter speed $10 \mu\text{s}$) with a frame rate of 50 frames per wing stroke period. PIV flow was seeded with oil particles generated by a particle generator (TSI) in an enclosed chamber unaffected by environmental disturbances. PIV flow fields were measured using the open source OpenPIV package [27]. A hot-wire anemometer (the Kanomax Anemomaster) was placed 3 ± 1 mm behind the flapping wings and the flow reading was recorded via analog voltage. The anemometer time constant was 1 s and we performed tandem flapping experiments for 10 s to achieve steady state.

Tandem wing experiments consisted of flapping the wing pairs at variable phase offset ϕ , frequency f , wing separation distance D^* , and amplitude θ_M . The downstream wing was actuated at $\theta(t) = \theta_M \sin(2\pi ft)$, and the upstream wing actuated at $\theta(t) = \theta_M \sin(2\pi ft + \phi)$. The wing separation distance, D^* , is defined as the distance from the trailing edge of the upstream wing to the leading edge of the downstream wing. In all instances, variables marked with an * are dimensionless values normalized by their respective dimensional values. We normalized wing separation distance D^* by the wingspan (1.4 cm). The upstream wing was mounted to a translation stage which allowed variation of the wing separation distance from 1 to 30 mm [Fig. 1(c)]. To compare the outflow speeds generated by tandem wing pairs with those generated by two isolated, flapping wings, we normalize the measured

outflow speed by the airspeed generated from the trailing wing alone and report normalized tandem airspeed as v^* . An experimental trial began with a measurement of the independent airspeed from each wing followed by a variation of wing kinematics.

Outflow observations.—Tandem wings generated a fast-moving jet of air surrounded by slower moving air entrained by the jet [Fig. 1(d)]. The non-normalized outflow speed varied between approximately 0.1–2 m/s, depending on the kinematic parameters. Temporal variation in the profile of the mean outflow speed (averaged spatially over the fast-moving jet) was small, with variations of approximately 10% of the mean airspeed [Fig. 1(e)].

Normalized outflow speed v^* was sensitive to both ϕ and D^* , and it varied by more than twofold in magnitude at the closest wing separation [$D^* = 0.2$; inset, Fig. 2(a)]. A comparison of outflow speed from the tandem wing pair versus the summed outflow speed from each wing flapping in isolation shows that nonlinear constructive and destructive interference in v^* occurred [inset, Fig. 2(a)]. For constructive phasing [negative ϕ in the inset of Fig. 2(a)], optimum v^* exceeded the linear superposition of the two wings run independently. For destructive phasing [positive ϕ in the

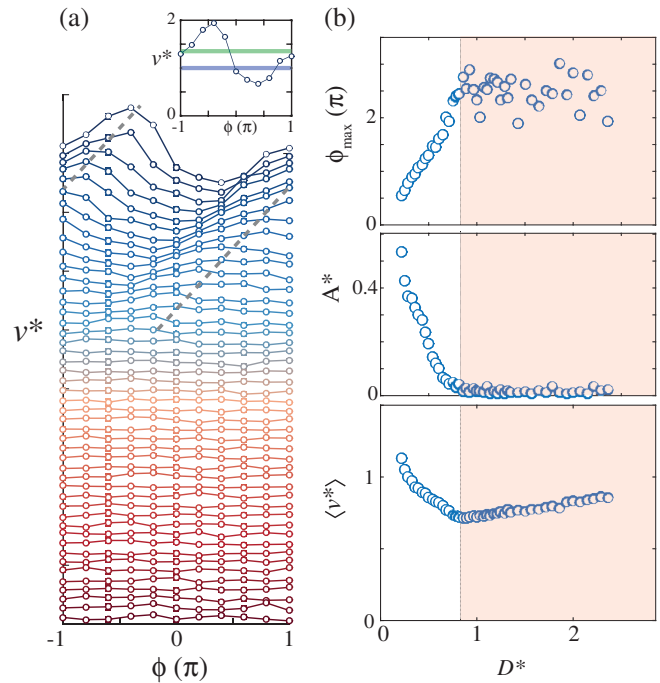


FIG. 2 (color online). Phase and distance effects on v^* . (a) Curves for constant distance and varied phase displayed in vertical order with increasing distance downward. Inset shows v^* versus ϕ for $D^* = 0.2$. The blue horizontal line indicates the value for the single wing, and the green horizontal line indicates the combined flow speed from linear superposition of the front and rear wings. (b) Optimum phase, ϕ_{\max} (top panel), aerodynamics coupling amplitude, A^* (middle panel), and phase-averaged airflow speed, $\langle v^* \rangle$ (bottom panel).

inset of Fig. 2(a)], tandem wing outflow velocities were lower than what would be obtained from the two wings run independently.

As separation distance increased, the effect of wing phasing decreased [Fig. 2(a)]. We fit $v^*(\phi, D^*)$ curves with the sinusoidal function $v^* = A^* \sin(\phi + \phi_{\max}) + \langle v^* \rangle$, where the fit variables (A^* , ϕ_{\max} , and $\langle v^* \rangle$) represent the optimum phase ϕ_{\max} , the phase-averaged airspeed $\langle v \rangle$, and the amplitude of the flow coupling A^* [Fig. 2(b)]. We unwrap the optimum phase ϕ_{\max} [28] and find that ϕ_{\max} linearly increased with D^* [Fig. 2(b) and illustrated by the dashed lines in Fig. 2(a)]. The coupling amplitude, A^* , decreased monotonically with D^* and vanished near $D^* = 1$, indicating that beyond wing separation distances of one wingspan, the outflow airspeed was largely unaffected by ϕ . However, we observed that the mean outflow speed was affected by D^* over the full experimental range, with v^* decreasing as D^* increases from zero to one, exhibiting a minimum at $D^* \approx 1$, and increasing for $D^* > 1$.

Flow interaction modes.—Variation in D^* results in three distinct flow regimes (Fig. 3). We hypothesize that these regimes are due to the spanwise component of the wing downwash, in which the downstream flow tends to diverge

radially away from the rotation axis of the stroke plane [Fig. 1(d)]. When wings are in close proximity, the trailing wing is in the downwash of the leading wing, and wing-wing interactions may occur [regime (i) in Fig. 3(b)]. However, when wing separation is large, the spanwise flow directs the downwash radially away from the downstream wing; in this regime no interaction occurs [(iii) in Fig. 3(b)]. In the intermediate regime the downstream wing is in a region of flow recirculation generated by the diverging flow of the upstream wing (see the Supplemental Material [26], video 3). In this regime [(ii) in Fig. 3(b)] wing-wing interactions are inhibited (since the trailing wing is outside of the downwash) and the outflow from the second wing is decreased due to the flow recirculation across the second wing.

The transitions between the three flow regimes depend on the details of the velocity profile behind the leading wing. We used PIV flow measurements to characterize the flow profile behind the leading wing (see Fig. 3 and the Supplemental Material [26], videos 1 and 2). We performed PIV measurements of the flow behind a single wing with the laser plane placed at varied increments along the spanwise direction normal to the midstroke angle. Using the anemometer, we measured the average flow velocity behind this single wing as a function of downstream distance. These measurements showed that the flow speed decays exponentially in the downstream direction (Supplemental Material [26], Fig. 2), supporting our findings that flow coupling may only occur up to a certain wing separation distance.

We evaluated the three-dimensional flow profile behind the wing along the x^*-y^* [Fig. 3(b), top] and x^*-z^* [Fig. 3(b), bottom] directions. In both planes, we observed that the outflow speed (v_x) is small near the wing root location and exhibited a maximum that traveled away from the wing root as the flow traveled downstream [the dashed lines in Fig. 3(b)]. The outflow direction diverges away from the central downstream axis indicating that for wing coupling to occur between wings the trailing wing must be placed close enough such that it is within the outflow envelope to enable vortex interaction. Examining the outflow envelope for the flapping wings in our experiment, we observe that at downstream distances greater than $D^* \approx 1$, the envelope is greater than unity (for the x^*-z^* plane, and 0.5 for the x^*-y^* plane), indicating that a portion of the flow is beyond the flapping envelope for a wing placed downstream beyond $D^* \approx 1$.

Flow optimization.—When wings are in close proximity, fluid flow may interact constructively or destructively. We hypothesized that the constructive and destructive interference observed at low D^* [Fig. 2(a)] is due to wing-wake interactions between the tandem wings as observed in other tandem wing systems [13–18]. Insect wings flapping at high angles of attack and stroke angles retain an attached leading-edge vortex [Fig. 4(a)] and shed a counterrotating vortex into the wake. This counterrotating vortex sheds

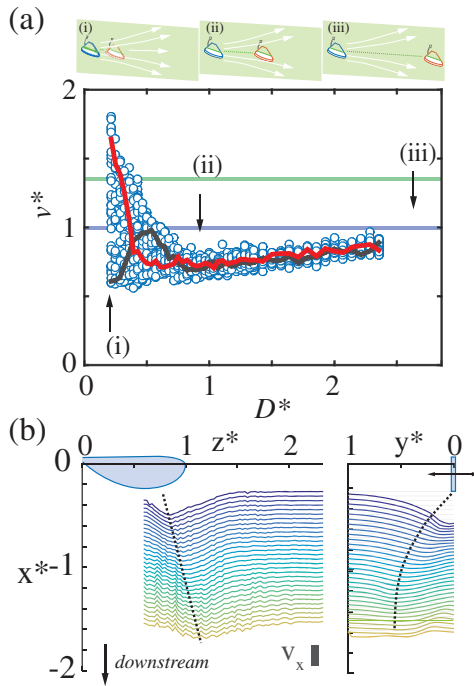


FIG. 3 (color online). (a) Airspeed versus D^* (bottom panel) and illustrations of flow at three distances (top panels). Red and black curves show a constant phase for best (the red line) and worst (the black line) fanning kinematics at closest separation. The blue horizontal line indicates the value for a single wing, and the green horizontal line indicates the combined flow speed from linear superposition of the front and rear wings. (b) Single wing flow field. View in the fore-aft direction with wing stroke in and out of the page (left panel) and lateral view (right panel). Spatial units are normalized by wing radius.

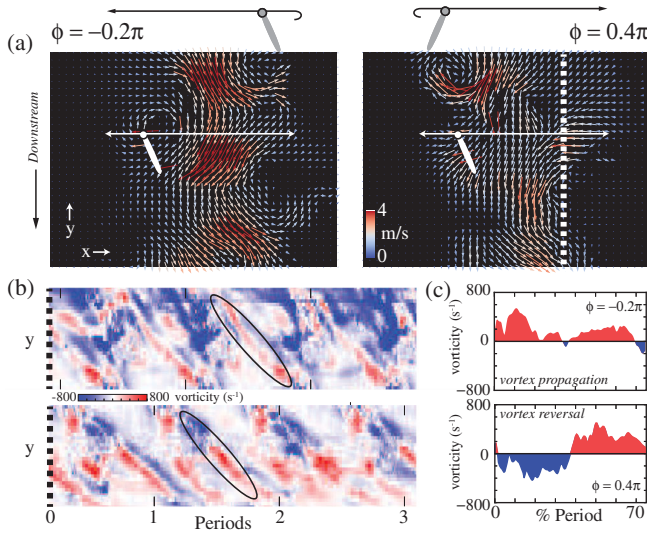


FIG. 4 (color online). (a) Lateral view of tandem wing airflow in PIV for optimal (left image, $\phi = -0.2\pi$) and suboptimal (right image, $\phi = 0.4\pi$) tandem fanning ($D^* = 0.46$). The range of the wing strokes is shown by lines. Vorticity profiles measured along the white dashed line (in the right image). (b) Downstream vorticity profiles versus stroke period evaluated along the dashed white line in (a). (Top image) Vorticity profile for $\phi = -0.2\pi$. (Bottom image) Vorticity profile for $\phi = 0.4\pi$. (c) Vortex magnitude evaluated along the advection paths highlighted by ellipses in (b).

from the trailing edge of the wing as a sheet, which separates a region of high-speed flow on one side of the wing from a region of low-speed flow on the other side. If the trailing wing advances through the high-speed flow associated with the vortex sheet of the leading wing such that the high-speed side of the vortex sheet is accelerated further by the motion of the second wing, then constructive interference will occur and the vortex sheet will be propagated. However, if the trailing wing advances through the vortex sheet such that the wing face is normal to the high-speed flow, the wing will decelerate the high-speed flow from the leading wing and the outflow speed will be decreased, consistent with destructive interference.

We visualize the vortex advection process for two phase offsets in Fig. 4(b) (and the Supplemental Material videos 1 and 2 [26]). At optimal phasing ($\phi = -0.2\pi$), we find that the vortex sign and the magnitude along the downstream direction are conserved. We highlight a propagating vortex in Fig. 4(b) (the ellipse in the top image) and plot the magnitude of the vortex as it propagates from the lead wing to the trailing wing [the top panel in Fig. 4(c)]. At suboptimal phasing ($\phi = 0.4\pi$) where outflow speed is low (see the Supplemental Material [26], Fig. 1), we find that the vortex reverses sign as it passes through the stroke plane of the second wing [the bottom image and panel in Figs. 4(b) and 4(c), respectively]. These observations directly show the destruction or propagation of the vortex shed from the leading wing onto the trailing wing.

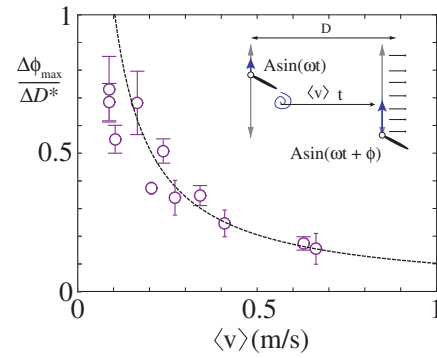


FIG. 5 (color online). Slope of optimum phase versus distance curves as a function of $\langle v \rangle$. Dashed line is fit from vortex capture model $\phi_{\max}/\Delta D^* = a/\langle v \rangle$ with $a = 0.10 \pm 0.01$ m/s. Inset shows schematic of model.

We parametrize the vortex interaction as a function of wing spacing, D^* , flow advection speed, and phase difference. Shed vortices created at time t travel at a speed $\langle v^* \rangle$ from the first wing over a distance D^* . Flow enhancement occurs when the second wing is in the same vertical position as the shed vortex when it reaches the trailing wing stroke plane. From the kinematic relationship of vortex advection, $D^* = \langle v^* \rangle t$, flow enhancement will occur when the elapsed time is $t = \phi/(2\pi f)$. Thus, solving for the phase-flow relationship we find

$$\phi_{\max} = \frac{2\pi f}{\langle v^* \rangle} D^*. \quad (1)$$

To test this model of vortex capture, we experimentally vary the advection speed, $\langle v^* \rangle$, by varying the wing oscillation amplitude. We measure the phase varying outflow speed, v^* , at varied D^* , ϕ , and $\langle v^* \rangle$ to determine ϕ_{\max} . Consistent with Fig. 2(b), we find that increasing D^* results in a linear increase in ϕ_{\max} . We fit lines to ϕ_{\max} versus D^* curves and measure the slope of this relationship, $\Delta\phi_{\max}/\Delta D^*$. Consistent with Eq. (1), we observe that increasing $\langle v^* \rangle$ leads to a decrease in $\Delta\phi_{\max}/\Delta D^*$ which was well fit by the prediction from our vortex advection model [Fig. 5].

Thus, through direct observation of the leading-edge vortex propagation (Fig. 4) and modulation of the vortex advection speed, we find that tandem wings interact constructively or destructively through vortex capture. These observations illustrate that fluid flow from collective wing arrays may be varied by varying the wing separation distance and the flapping kinematics (ϕ or $\langle v^* \rangle$).

Conclusion.—Collective fluid-structure interactions are common in biological and natural systems; however, most studies to date have explored collective flow enhancement at low Reynolds numbers, or thrust enhancement at high Reynolds numbers. Through experiments on flapping wings at moderate Reynolds numbers, we find that wings flapping in tandem are capable of working constructively to

generate airflows that are faster than the summed airflows expected from individual contributions of each wing. The optimum phase at which maximum outflow occurs can be modulated by the kinematic parameters, including phase, frequency, and stroke amplitude (which controls mean flow speed), according to a simple model. The potential to increase outflow speeds by flapping wings in tandem, in combination with previous results indicating power savings for tandem wings [14] may have important implications for biological and industrial systems. Considering that honeybee ventilation depends on mass-flow rate, further study of the full three-dimensional flow fields by wing arrays will be necessary. Fluid-mechanical interactions among tandem flapping wings can lead to nonlinear enhancement of downstream airspeed and provides a rich system for studying fluid-structure interactions at intermediate Reynolds numbers.

We acknowledge funding support from the Wyss Institute for Biologically Inspired Engineering. N. G. acknowledges funding from the James S. McDonnell postdoctoral fellowship in complex systems. J. M. P. was funded by a NSF graduate research fellowship.

-
- [1] S. Vogel, *Life in Moving Fluids: The Physical Biology of Flow* (Princeton University Press, Princeton, NJ, 1996).
- [2] M. Gazzola, M. Argentina, and L. Mahadevan, *Nat. Phys.* **10**, 758 (2014).
- [3] A. L. Eberle, P. G. Reinhall, and T. L. Daniel, *Bioinspiration Biomimetics* **9**, 025005 (2014).
- [4] K. L. Feilich and G. V. Lauder, *Bioinspiration Biomimetics* **10**, 036002 (2015).
- [5] A. M. Mountcastle and S. A. Combes, *Proc. R. Soc. B* **280**, 20130531 (2013).
- [6] T. Nakata and H. Liu, *J. Comput. Phys.* **231**, 1822 (2012).
- [7] O. H. Shapiro, V. I. Fernandez, M. Garren, J. S. Guasto, F. P. Debaillon-Vesque, E. Kramarsky-Winter, A. Vardi, and R. Stocker, *Proc. Natl. Acad. Sci. U.S.A.* **111**, 13391 (2014).
- [8] A. Vilfan and F. Jülicher, *Phys. Rev. Lett.* **96**, 058102 (2006).
- [9] R. Ma, G. S. Klindt, I. H. Riedel-Kruse, F. Jülicher, and B. M. Friedrich, *Phys. Rev. Lett.* **113**, 048101 (2014).
- [10] J. Tailleur and M. E. Cates, *Phys. Rev. Lett.* **100**, 218103 (2008).
- [11] S. J. Portugal, T. Y. Hubel, J. Fritz, S. Heese, D. Trobe, B. Voelkl, S. Hailes, A. M. Wilson, and J. R. Usherwood, *Nature (London)* **505**, 399 (2014).
- [12] D. Weihs, *Nature (London)* **241**, 290 (1973).
- [13] D. Rival, D. Schonweitz, and C. Tropea, *Bioinspiration Biomimetics* **6**, 016008 (2011).
- [14] J. R. Usherwood and F.-O. Lehmann, *J. R. Soc. Interface* **5**, 1303 (2008).
- [15] F.-O. Lehmann, *Exp. Fluids* **46**, 765 (2009).
- [16] Z. J. Wang and D. Russell, *Phys. Rev. Lett.* **99**, 148101 (2007).
- [17] T. M. Broering and Y.-S. Lian, *Acta Mech. Sin.* **28**, 1557 (2012).
- [18] R. W. Whittlesey, S. Liska, and J. O. Dabiri, *Bioinspiration Biomimetics* **5**, 035005 (2010).
- [19] M. Kremien, U. Shavit, T. Mass, and A. Genin, *Proc. Natl. Acad. Sci. U.S.A.* **110**, 8978 (2013).
- [20] D. B. Araya, A. E. Craig, M. Kinzel, and J. O. Dabiri, *J. Renewable Sustainable Energy* **6**, 063118 (2014).
- [21] W. B. Hobbs and D. L. Hu, *J. Fluids Struct.* **28**, 103 (2012).
- [22] H. K. Ma, H. C. Su, and W. F. Luo, *Sens. Actuators, A* **189**, 356 (2013).
- [23] E. E. Southwick and R. Moritz, *J. Insect Physiol.* **33**, 623 (1987).
- [24] T. D. Seeley, *J. Insect Physiol.* **20**, 2301 (1974).
- [25] J. P. Whitney, P. S. Sreetharan, K. Y. Ma, and R. J. Wood, *J. Micromech. Microeng.* **21**, 115021 (2011).
- [26] See Supplemental Material at <http://link.aps.org/supplemental/10.1103/PhysRevLett.115.188101> for further results and PIV video of fluid-flow.
- [27] Z. J. Taylor, R. Gurka, G. A. Kopp, and A. Liberzon, *IEEE Trans. Instrum. Meas.* **59**, 3262 (2010).
- [28] Phase unwrapping consists of adding 2π to ϕ_{\max} when discontinuities greater than 2π occur (as happens when phase wraps around from $-\pi$ to π).